RSS Technical Report No. 05262022 **05/26/2022**

The Microwave Climate Data Center Repository

Katherine Wentz

Research Scientist, Remote Sensing Systems

Andrew Manaster

Research Scientist, Remote Sensing Systems

Remote Sensing Systems

444 Tenth Street, Suite 200, Santa Rosa, CA 95401 (707) 545-2904

The Microwave Climate Data Center Repository

Katherine Wentz[1*] and Andrew Manaster[1]

[1] Remote Sensing Systems, 444 Tenth Street, Suite 200, Santa Rosa, CA 95401
[*] Corresponding author(s): Katherine Wentz (kwentz@remss.com)

Abstract: Since 1979, Remote Sensing Systems has been providing a global community of researchers and decision makers with inter-calibrated microwave measurements and geophysical retrievals derived from passive and active spaceborne sensors. These datasets, from 35 microwave sensors covering a time period of 40 years, have been consolidated at the Microwave Climate Data Center repository. The geophysical retrievals include: sea-surface temperature, near-surface ocean wind speed and direction, columnar atmospheric water vapor, columnar cloud liquid water, sea-surface rain rate, sea-surface salinity, and atmospheric temperature profiles. Consistent calibration procedures and retrieval methods have been applied during the data processing to ensure these datasets are suitable for climate research. All of the geophysical retrievals relate to the air-sea boundary layer and are classified as essential climate variables by the Global Climate Observing System. In this paper, we give an overview of the microwave sensors, the inter-calibration methods, the retrieval algorithms, and the air-sea essential climate variable datasets housed at the Microwave Climate Data Center.

Keywords: Microwave Climate Data Center; Remote Sensing; Air-Sea Essential Climate Variables; Sensor Inter-Calibration; Radiative Transfer Model; Maximum Likelihood Estimator; Validation

Background and Summary

In the electromagnetic spectrum, microwave (MW) frequencies range from approximately 0.3 to 300 GHz (wavelengths between one millimeter and one meter). This MW radiation, whether emitted passively by various sources including the Sun and Earth or actively by radar that sends out pulses of radiation, interacts in unique ways with the Earth's surface and atmosphere[1]. Instruments designed to measure radiation at MW frequencies onboard Earth-orbiting satellites are used to retrieve geophysical quantities that are crucial for understanding the world's weather and climate. In this regard, Remote Sensing Systems (RSS) has focused on a specific area of research and data production: passive and active MW observations of the world's oceans. Using frequently updated retrieval algorithms, RSS translates the MW radiation observed by satellites into climate-quality data. These datasets are publicly available and hosted by the RSS Microwave Climate Data Center (MCDC) repository at https://www.remss.com.

MCDC Datasets include: sea-surface temperature, near-surface ocean wind speed and direction, columnar atmospheric water vapor, columnar cloud liquid water, sea-surface rain rate, sea-surface salinity, and atmospheric temperature profiles. All of these climate datasets are considered air-sea (AS) variables and are classified as essential climate variables (ECVs) by the Global Climate Observing System (GCOS)[2]. Most of these global geophysical datasets, hereafter referred to as AS-ECVs, extend from 1987 to the present day.

While there are many ways to observe AS-ECVs over the ocean, using spaceborne MW sensors to do so provides distinct advantages over other forms of measurement. First, the atmosphere is relatively transparent at many MW frequencies. This allows spaceborne MW sensors to observe the surface of the Earth even in areas of heavy cloud cover or high columnar water vapor. Around 22 and 60 GHz, the atmosphere becomes opaque to MW radiation; nonetheless, these MW frequencies can be used for measuring geophysical qualities of the intervening atmosphere. Secondly, MW sensors do not require solar illumination to observe the Earth's surface and atmosphere, and therefore they can take measurements at any time of the day making them well-suited for observing diurnal cycles in AS-ECVs. Infrared (IR) imagers can similarly take snapshots of clouds throughout the day; however, they can only image the tops of clouds. Third, polar orbiting MW sensors are able to view wide swaths of the Earth over the course of a single day and can provide global coverage every few days. This is in contrast to airborne, ship, or other ground-based measurements which can only provide information at a single point or within a relatively small area[3].

Despite the advantages of MW remote sensing, there are two primary limitations to using spaceborne MW instruments to measure AS-ECVs over the world's oceans. First, the presence of heavy rain interferes with MW radiation at higher frequencies (> ~12 GHz) because rain drops attenuate and scatter MW signals while also creating splash effects that are difficult to disentangle from the AS-ECV signals of interest[4,5]. Second, MW sensors have a relatively coarse spatial resolution as compared to higher frequency bands of radiation, such as visible and IR. To increase the spatial resolution, the MW frequency must be increased or a larger antenna needs to be used[1,3]. Unfortunately, some AS-ECVs, such as salinity, are only sensitive at the lower frequencies (1.4 GHz). Given these limitations, RSS uses MW satellite sensors to retrieve AS-ECVs in ocean areas that are generally free of heavy rain and assumes that the AS-ECVs are relatively constant at kilometer scales. However, there are several exceptions to this, which are discussed in greater detail in this paper.

RSS has 40+ years of experience in generating and refining the MCDC AS-ECV products from MW sensors. As a result, RSS has developed a reputation for providing precisely calibrated AS-ECVs that can be used for the most demanding climate-trend analyses. This trust is based on the high-degree of consistency in all aspects of data production, starting with sensor inter-calibration, continuing through to the advanced radiative transfer models and geophysical model functions in the RSS retrieval algorithms, and ending with rigorous validation analyses. The goal of this paper is to provide the community with a detailed description of the generation and current status of AS-ECV datasets hosted by the RSS MCDC repository.

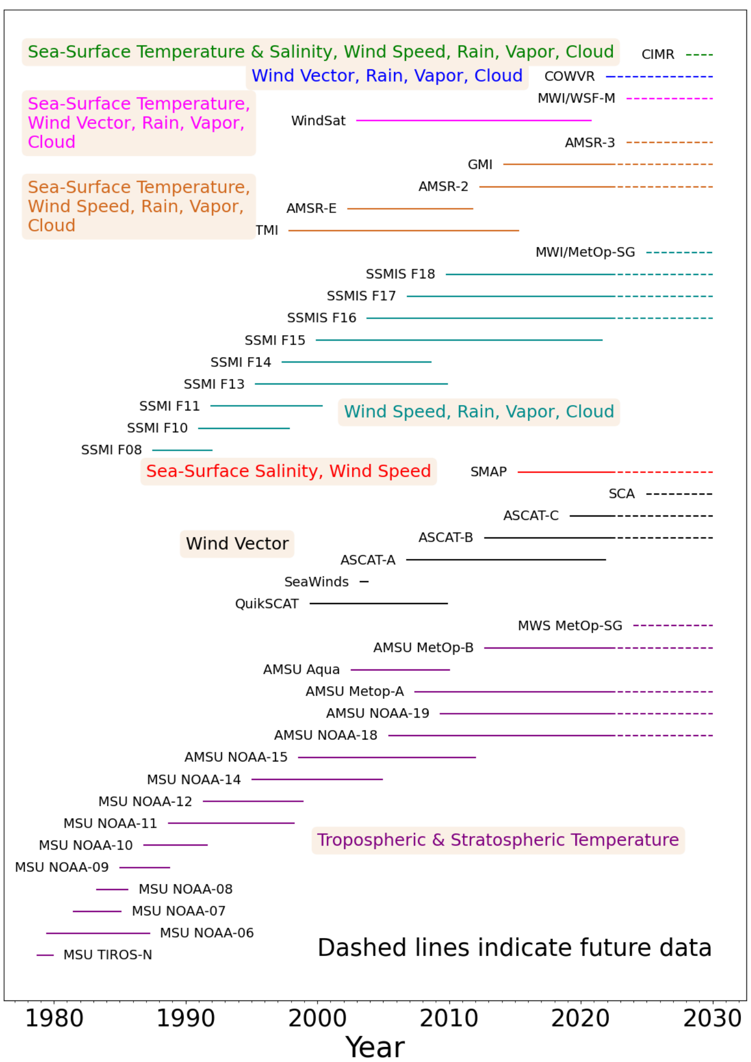

Figure 1 MCDC Microwave Sensor Collection. Microwave sensors with their mission timelines that are used in constructing the MCDC AS-ECV data records.

Methods

MW Sensor Inventory

The MCDC AS-ECV sensor inventory currently includes 35 MW sensors covering a time period of 40 years. Measurements from these sensors have been inter-calibrated and processed using consistent data processing techniques for: (1) resampling, (2) geolocation, and (3) AS-ECV retrievals. Figure 1 shows the mission timelines for the sensors, and Tables 1–3 provide the instrument characteristics. The following additional sensors will be added in the near future: CIMR, COWVR, MWI/WSF-M, AMSR-3, MWI/Metop-SG, SCA, and MWS/Metop-SG.

There are three basic types of sensors:

1. The conical scanning MW imager (Table 1)
2. The cross-track scanning MW sounder (Table 2)
3. The scatterometer (both conical scanning and fixed cross-track) (Table 3)

The MW imagers and sounders are radiometers that observe the upwelling brightness temperature (T_B) that is passively emitted from the Earth. The scatterometers are active radars that transmit power to the Earth and then measure the received power, reporting the normalized radar cross-section (σ_o). Both radiometer and scatterometer MW sensors fly in polar orbits with varying degrees of inclination. The trajectory of a slightly inclined near-polar orbit is nearly north–south, with the satellite passing near the Earth poles each orbit. At the equator, the near-polar orbiters are sun-synchronous and cross the equator at the same local mean solar time with ascending and descending orbit segments having local equatorial crossing times that are approximately 12 hours apart. The local equator crossing time slowly drifted for some of the early sensors, for which orbit maintenance was not done. These near-polar orbiters roughly orbit the Earth 14 times a day, every 90 minutes. On the other hand, a highly inclined orbit ground trajectory does not reach the North and South poles, but rather, covers a smaller latitude band (e.g., 40°S to 40°N for TMI and 60°S to 60°N for GMI) than near-polar orbiters. Sensors in inclined orbits view the Earth at different times of the day, precessing through the entire diurnal cycle and providing greater coverage at lower latitudes. Depending on the swath width of the sensor, it takes two to four days for the sensor to provide full longitudinal coverage.

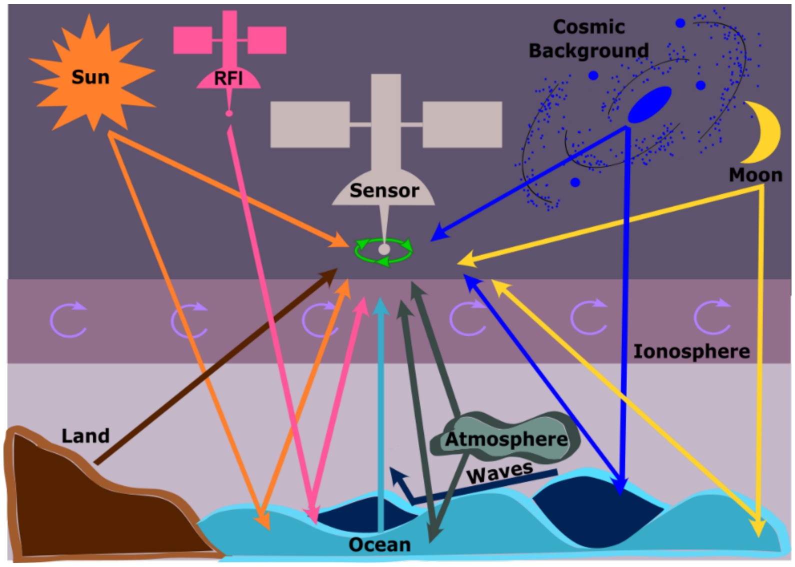

Figure 2 Inputs to Observed Microwave Brightness Temperature (T_B). The arrows show the various components that contribute to the observed T_A and top-of-the-atmosphere T_B.

The MW imager and sounder retrieval algorithms require the top-of-the-atmosphere T_Bs calculated from the observed antenna temperature (T_A) for each MW polarization and frequency (Equation 1; Table 4). The T_A is converted to top-of-the-atmosphere T_B by removing cold space spillover onto the sensor field of view and polarization contamination from orthogonal polarizations, i.e., cross-polarization (Equations 1–4; Table 4). Equation (2) accounts for the additional radiative input from an emissive reflector in the case of SSMI/S, TMI, and SMAP sensors. Before applying the retrieval algorithm, extraneous sources of radiation contributing to observed T_A (and, subsequently, observed top-of-the-atmosphere T_B) must be identified. In most AS-ECV retrievals, these sources include land or sea ice within the antenna field of view as well as radio frequency interference (RFI). For the salinity retrievals, additional extraneous radiation sources include cosmic MW background, sun, moon, and galaxy, either viewed directly through the antenna or through the reflection from the ocean surface. In addition, at the 1.4 GHz frequency required for the salinity algorithm, the ionosphere rotates the polarization vector of the radiation traveling through it due to the Faraday effect[6]. Polarization rotation also needs to be considered for fully polarimetric imagers like WindSat, although its higher frequencies are less affected by the rotation. To remove the ionosphere effects from the observed top-of-the-atmosphere T_B, an ancillary dataset of total electron content (TEC) is used to correct the T_B as it passes through the ionosphere. Figure 2 shows how these spurious contamination sources contribute to the overall T_A and top-of-the-atmosphere T_B observation.

$$\begin{pmatrix} T_{B,v} \\ T_{B,h} \end{pmatrix} = \mathbf{A}^{-1} \begin{pmatrix} T'_{A,v} \\ T'_{A,h} \end{pmatrix} = \frac{1}{\det(\mathbf{A})} \begin{pmatrix} 1-\chi_{hv} & -\chi_{hv} \\ -\chi_{vh} & 1-\chi_{vh} \end{pmatrix} \begin{pmatrix} T'_{A,v} \\ T'_{A,h} \end{pmatrix} \tag{1}$$

$$T'_{A,p} = \frac{T''_{A,p} - E_{refl,p} T_{refl}}{\left(1 - E_{refl,p}\right)} \quad p = v, h \; polarization \tag{2}$$

$$T''_{A,p} = \frac{T_{A,p} - \left(1 - \eta_p\right) T_C}{\eta_p} \quad p = v, h \; polarization \tag{3}$$

$$\det(\mathbf{A}) = (1 - \chi_{vh})(1 - \chi_{hv}) - \chi_{vh}\chi_{hv} \tag{4}$$

MW Sensor Inter-Calibration

According to the National Research Council, a climate data record (CDR) is defined as “a time series of measurements of sufficient length, consistency, and continuity to determine climate variability and climate change”[7]. In order for the data products to reach the consistency required to build a climate-quality dataset, covering two to four decades, the basic measurements (T_B or σ_o) need to be precisely inter-calibrated. Given the 35 MW sensors in the MCDC inventory, inter-calibration has been a major component of the work done at RSS.

RSS performed the first MW imager inter-calibration in 1990 when the second SSM/I went into operation. Since then, there have been many generations of calibration procedures[8,9,10,11,12]. Currently, 14 MW imagers, excluding one of the SSMIS', have been inter-calibrated to GMI which provides the most accurate measurements with a T_B absolute accuracy of 0.25 K and a T_A absolute accuracy of 0.1 K valid from cold ocean temperatures to the hot rainforest[12]. Moreover, GMI is in an inclined orbit and provides coincident collocations with other sensors, essentially eliminating errors related to diurnal variations.

The MW sounder T_Bs are a self-consistent dataset and are not inter-calibrated with the imagers because the 50–60 GHz observations taken by the sounders are fundamentally different than the T_B measurements taken by the imagers. MW sounders are inter-calibrated by comparing co-orbiting satellite measurements of top of the atmosphere T_Bs from MSU and AMSU. Moreover, the difference between MSU and AMSU measurements are averaged and then subtracted from the AMSU data so that co-orbiting MSU and AMSU T_Bs match one another[13]. In addition, the MW sounder inter-calibration solves for differences in the earth incidence angle (EIA), diurnal drift, and weighting functions between MSU and AMSU[14,15].

Buoy wind speeds (< 15 m/s) and dropsondes (≥ 15 m/s) are the ultimate calibration standard for scatterometer wind speed retrievals. WindSat wind speeds have been validated against buoys and dropsondes in rain-free conditions, and now WindSat serves as a consistent reference for scatterometer wind retrievals. Adjustments are made to the σ_o measurements to obtain agreement between the imager and scatterometer wind speed retrievals. For scatterometer wind direction retrievals, the National Center for Environmental Prediction (NCEP) Global Data Assimilation System (GDAS) was used as the calibration standard. Direct comparisons between contemporaneous scatterometers are also used in the inter-calibration procedure[16].

MW Imager AS-ECV Retrieval Algorithm

The seven AS-ECVs that are retrieved by the MW imager algorithm are:

1. Sea-surface temperature
2. Ocean wind speed at 10 m above surface
3. Ocean wind direction at 10 m above surface
4. Columnar atmospheric water vapor above the ocean
5. Columnar cloud liquid water above the ocean
6. Sea-surface rain rate
7. Sea-surface salinity

The retrieval algorithm for the MW imagers is based on a radiative transfer model (RTM) for the earth and attenuating atmosphere, which is common to all of the imagers. The RTM is also called the forward model because it provides top-of-the-atmosphere T_Bs for a given earth scene when AS-ECVs are used as inputs (Equations 5–10; Table 4). The essential elements of the RTM are surface temperature (T_S) and emissivity (E), as well as atmospheric profiles of pressure (P), temperature (T), water vapor (ρ_V), and cloud liquid water (ρ_L). The emissivity is a function of surface temperature, sea-surface salinity (S), wind speed (W), and wind direction relative to the azimuthal look (φ). The rain rate is a function of the RTM-derived cloud liquid water and the rain column height, which in turn is linearly related to RTM-derived sea-surface temperature; generally speaking, rain occurs when the cloud liquid water value exceeds a threshold of 0.18 kg/m^2. In the sea-surface salinity retrieval, there is only one frequency available (1.4 GHz); therefore, the RTM requires several ancillary datasets to retrieve emissivity and top-of-the-atmosphere T_B, including sea-surface temperature, wind speed and direction, atmospheric profiles, and rain rate[17]. The RTM is described in greater detail in the literature[18,19,20,21] and provided for cases in which the atmospheric scattering by liquid water droplets is neglected[22,23,24].

$$T_B = T_{BU} + \tau(0,H)[ET_S + (1-E)(T_{BD} + \tau(0,H)T_C)] + \tau(0,H)T_{B,scat} \tag{5}$$

$$T_{B,scat} = \Omega(1-E)[T_{BD} + \tau(0,H)T_C - T_C] \tag{6}$$

$$T_{BU} = \sec\theta \int_0^H \alpha(h)T(h)\tau(h,H)dh,\ \ T_{BD} = \sec\theta \int_0^H \alpha(h)T(h)\tau(0,h)dh \tag{7}$$

$$\tau(h_1,h_2) = \exp\left(-\sec\theta \int_{h_1}^{h_2} \alpha(h)dh\right) \tag{8}$$

$$\alpha(h) = \alpha_D(T(h),P(h)) + \alpha_V(T(h),P(h),\rho_V(h)) + \alpha_L(\varepsilon_L,\rho_L(h)) \tag{9}$$

$$E = E_0(\theta,S,T_S) + \Delta E_W(\theta,W,T_S) + \Delta E_\varphi(\theta,W,\varphi) \tag{10}$$

The retrieval algorithm is an approximate inversion of the forward model. It provides estimates of the AS-ECVs for a given set of top-of-the-atmosphere T_B observations taken over a range of frequencies and polarizations. The retrieval algorithm uses multiple non-linear regressions in order to find the AS-ECVs[18,25]. The regression coefficients are derived from a training set of simulated T_Bs from the RTM using Monte Carlo combinations of AS-ECVs representative of all-possible global conditions. To deal with a possible non-linear dependence between the T_B and AS-ECV, a two-stage linear regression is used (Equations 11–13, using two AS-ECVs as an example; Table 4). The first stage (m_{1j}) is valid for global conditions and provides a first-guess for the AS-ECVs. Given this first guess, a second-stage regression (m_{2j}) is selected based on the specific environment found by the first stage.

$$m_{1j} = a_{0j} + \sum_{i=1}^{nMWchan} a_{ij}t_i + b_{ij}t_i^2 \tag{11}$$

$$m_{2j} = \sum_{k=k_0}^{k_0+1}\sum_{l=l_0}^{l_0+1} w_{k-k_0,l-l_0}\left(c_{0jkl} + \sum_{i=1}^{nMWchan} c_{ijkl}t_i\right) \tag{12}$$

$$t_i = T_{Bi} - 150 \ \text{ for all but 24 GHz},\ \ t_i = -\ln(290 - T_{Bi}) \ \text{ for 24 GHz} \tag{13}$$

An exception to the retrieval algorithm regression approach is used in the wind vector retrieval (wind speed and wind direction). In this case, the MW imager needs to be fully polarimetric and a classical "chi-squared" Maximum Likelihood Estimator (MLE) is used that minimizes the differences between the observed T_B and RTM-computed T_B. The wind direction algorithms generally, but not always, provide multiple solutions (ambiguities) for wind directions. The final step in the wind direction retrieval is an ambiguity selection that chooses the wind vector that is consistent with nearby values[26].

MW Sounder Atmospheric Temperature Retrieval Algorithm

The retrieval algorithm for the MW sounders finds the temperature for five atmospheric layers[27]:

1. Temperature of the Lower Troposphere (TLT)
2. Temperature of the Total Troposphere (TTT)
3. Temperature of the Middle Troposphere (TMT)
4. Temperature of the Troposphere and Stratosphere (TTS)
5. Temperature of the Lower Stratosphere (TLS)

The atmospheric temperature products are provided globally over ocean, land, and ice. This is in contrast to the other MCDC data products which are only provided over the global ocean. The sounding channels used in the retrieval are in the 50–60 GHz part of the MW spectrum. Since molecular oxygen in the atmosphere strongly absorbs and emits MW radiation in this range, the T_B at these frequencies represents the vertically-averaged air temperature over a select layer of the atmosphere. The extent and vertical location of the layer depends on the EIA and frequency of the observation. Equation (14) relates the observed T_B to the sum of the small surface contribution (first term) and the vertically-averaged atmospheric contribution (second term) (Table 4)[13]. The surface contribution to the T_B depends on the zenith optical depth (z) for an atmospheric layer, which is the integration of the atmospheric absorption coefficient (κ) (Equation 15; Table 4). Weighting functions in the second term are used to separate the T_B contributions from various layers in the atmosphere; they are a function of the height above sea level and depend on the observation frequency and the EIA (Equation 16; Table 4). For three of the channels (TMT, TTS, and TLS) we report the T_B for a limited set of near-nadir views, with each off-nadir T_B referred to nadir using adjustments calculated from the RTM for climatological atmospheric profiles. TTT is constructed from a weighted combination of TMT and TLS to reduce the stratospheric contribution[28]. TLT is constructed using a linear combination of measurements at different views to move the weighting function closer to the surface[14,15].

$$T_B = ET_S \exp(-z(0,\infty)\sec\theta) + \int_0^H F(h)T(h)dh \tag{14}$$

$$z(h_1,h_2) = \int_{h_2}^{h_1} \kappa(h)dh \tag{15}$$

$$F(h) = \kappa(h)\sec\theta\exp(-z(h,\infty)\sec\theta) + \kappa(h)\sec\theta\exp(-z(0,h)\sec\theta)(1-E)\exp(-z(0,\infty)\sec\theta) \tag{16}$$

MW Scatterometer Wind Vector Retrieval Algorithm

In low wind conditions, the smooth ocean surface reflects most of the microwave energy away from the scatterometer and there is very little backscatter returned to the sensor. However, wind-induced ocean surface roughness increases scatter in every direction off of the capillary waves. The amount of backscatter depends on surface wind speed (W) and wind direction relative to the azimuthal look (φ)[3]. The retrieval algorithm for the MW scatterometers measures the ocean wind vector (wind speed and wind direction) 10 meters above the ocean surface. The retrieval algorithm is based upon a geophysical model function (GMF) that relates σ_o to wind speed and direction[23,29,30]. The GMF is an expanded Fourier series of even harmonics in the relative wind direction (Equation 17, keeping harmonics up to the second order; Table 4). The coefficients for the fifth order polynomial of wind speed for each of the harmonic functions in the wind direction are tuned using wind speed measurements from WindSat and wind directions from NCEP that are both matched up with the scatterometer σ_o. Similar to the wind vector retrieval algorithm for fully polarimetric MW imagers, the scatterometer wind vector retrieval algorithm employs a classical "chi-squared" MLE that minimizes the differences between the observed σ_o and the GMF σ_o. The MLE is then followed by an ambiguity selection algorithm[26].

$$\sigma_o = \sum_{i=1}^{5} d_{0,i}W^i + \cos\varphi \sum_{i=1}^{5} d_{1,i}W^i + \cos(2\varphi)\sum_{i=1}^{5} d_{2,i}W^i \tag{17}$$

Data Records

The AS-ECVs hosted by the MCDC are used by the scientific community to study climate change, as well as by commercial and operational agencies for a variety of purposes, including weather operations, renewable energy, and shipping logistics. The MCDC AS-ECV datasets are freely available from the RSS website via both HTTP (https://data.remss.com/) and FTP file transfer protocols. Table 5 provides key specifications of individual AS-ECV datasets, the majority of which are on an Earth-centered grid at regular 0.25-degree latitude/longitude intervals with a daily or composite (3-day, weekly, 8-day, monthly) temporal resolution. Although the AS-ECVs are released on a 0.25-degree sampling grid, it is important to note that their inherent resolution in kilometers depends on the sensor (Tables 1–3). In addition to the individual AS-ECV datasets, intercalibrated top-of-the-atmosphere T_Bs from MW imagers are freely available upon request. The following subsections describe individual AS-ECV datasets as well as merged AS-ECV CDRs.

Sea-Surface Temperature

Sea-surface temperature (SST) is a measure of the temperature (°C) of the skin layer of the ocean (~20 μm-depths measured by IR imagers), sub-skin layer of the ocean (~1 mm-depths measured by MW imagers), and foundation ocean (0.5–1.5 m-depths). SST measurements are used to observe changes in global climate, monitor decadal climate variability including the El Niño Southern Oscillation (ENSO), and forecast tropical cyclones. SSTs are important boundary (input) conditions for atmosphere-only models and have been used to train coupled ocean-atmosphere climate models so that their outputs match observations[31]. Beyond climate modeling and seasonal forecasting, SST observations are useful for predicting coral bleaching, tracking pollution, and commercial fishery and tourism industries. The MCDC provides sub-skin SSTs from MW imagers with low frequency channels (6–11 GHz) that are sensitive to ocean temperatures at these depths. The MCDC also produces an optimally interpolated (OI) foundation SST, which merges observations from multiple sensors[32,33,34] and removes diurnal warming[35,36]. There are two flavors of the MCDC OI SST product. One of the OI SSTs only uses MW imagers as input, while the other employs both MW imagers *and* IR imagers that measure skin SST. MCDC SSTs range from -3 to 35°C.

Ocean Wind Speed and Wind Vectors over Ocean and Land

The MCDC repository of wind speed (m/s) and wind vectors (wind speed and direction in degrees) represent near-surface conditions (10 meters above the ocean surface). The wind direction is provided in the wind vector azimuth convention, i.e., the direction points along mass flow with 0 degrees referring to wind blowing towards the Northern direction (the degrees increase in the clockwise direction). On short timescales (daily to weekly), winds are used for predicting and monitoring tropical cyclones. On longer timescales (seasonal to interannual), winds can provide insight into climate variability, including monsoon intensity and changes in rain patterns (e.g., due to ENSO), which can greatly affect global populations in various parts of the world via flooding or droughts[37,38]. The MCDC provides scalar ocean wind speeds from MW imagers both in non-rainy conditions and rainy conditions (Tropical Cyclone (TC) winds and All-Weather winds[39,40,41]) (Figure 3). In addition, the MCDC distributes ocean wind vectors from fully polarimetric MW imagers, MW scatterometers as well as the Cross-Calibrated Multi-Platform (CCMP) wind vector analysis product[42,43]. Note that the MCDC supplies two wind speed products, one from low frequency MW imager observations (11–37 GHz) and the second from medium frequency MW imager observations (19–37 GHz). MCDC wind speeds range from 0 to 70 m/s and wind directions range from 0 to 350 degrees.

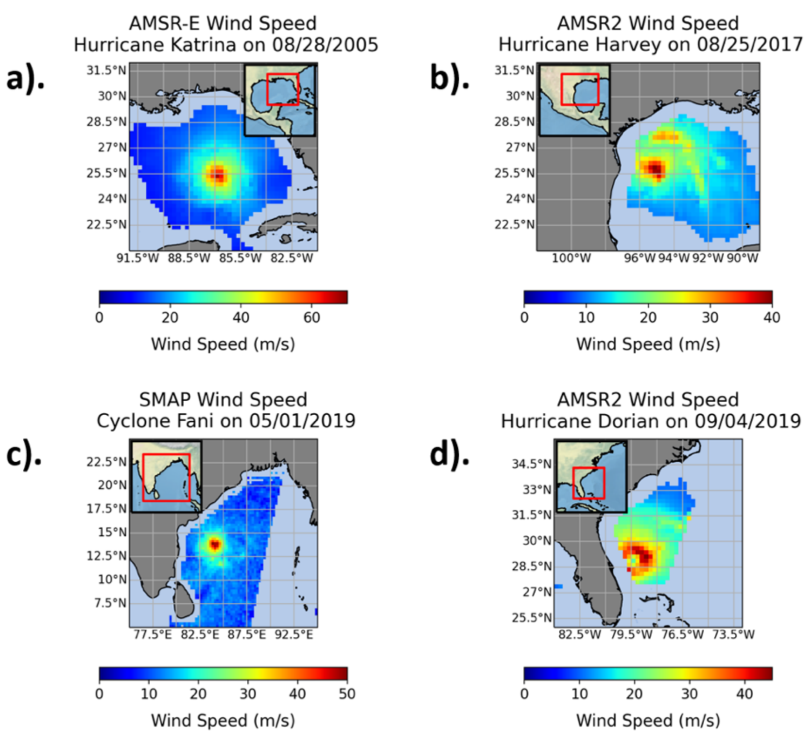

Figure 3 MCDC Tropical Cyclone (TC) Winds. Subplots show wind speeds in hurricanes and tropical cyclones for AMSR-E (a), AMSR-2 (b, d), and SMAP (c).

Columnar Atmospheric Water Vapor over Ocean

Columnar atmospheric water vapor is the amount of gaseous water present in a column of air extending from the Earth's surface to the top of the atmosphere. Columnar water vapor is reported in units of kg/m^2 (the vertically-integrated mass of water vapor), which can then be converted to mm when divided by the density of water. Atmospheric water vapor is essential for cloud formation and latent heat transport, both of which contribute to tropical and extratropical storms. In addition, evidence suggests that increased atmospheric moisture will enhance the intensity of atmospheric rivers, which will lead to substantially longer and wider atmospheric rivers than the ones observed today[44,45]. Water vapor also plays an important role in the climate due to its potency as a greenhouse gas and water vapor positive feedback loop. This water vapor feedback plus the temperature lapse rate feedback, 1.30 W m^{-2} °C^{-1} in total, will increase the total climate feedback warming by 50%[46,47]. The MCDC provides measurements of water vapor over the ocean calculated from the 22 GHz band of MW imagers, which is near the peak of one of the water vapor absorption frequencies; values range from 0 to 120 mm.

Columnar Cloud Liquid Water over Ocean

Columnar cloud liquid water is a measure of the depth of liquid water in mm contained in a cloud for a vertical column of the atmosphere (any ice and snow present in the cloud are not included in this measurement). Cloud liquid water is also often reported as the mass of liquid water per mass or volume of air (g/kg or g/m^3). Cloud liquid water plays a substantial role not only in the global water cycle, but also in how atmospheric radiation is absorbed, scattered, and reemitted: clouds can have competing effects on the climate, some of which cool the earth by reflecting visible light while others warm the earth by absorbing IR radiation[48]. The MCDC supplies cloud liquid water measurements above the ocean calculated from a range of MW imager frequencies (19–37 GHz); values range from 0 to 1.8 mm.

Sea-Surface Rain Rate

Sea-surface rain rate is a measure of the average rain rate at the ocean surface in mm/hr. Rain from atmospheric rivers and monsoons supplies fresh water to the world's population centers[49,50,51]. Over recent decades there has been a narrowing and strengthening of rain in the Inter-Tropical Convergence Zone (ITCZ), a belt of rainfall that shifts north and south, providing monsoonal rain[52]. Accurate measurements of rain improve characterization of droughts, landslides, floods, and severe storms, which have enormous impacts on society. The MCDC provides sea-surface rain rates calculated from a range of MW imager frequencies (19–37 GHz); values range from 0 to 25 mm/hr.

Sea-Surface Salinity

Sea-surface salinity (SSS) is a measure of how salty the ocean is in its uppermost layer (~1 cm). It is expressed in terms of Practical Salinity Units (psu), which are approximately equivalent to parts per thousand. Satellite measurements of SSS are important for studying the global water cycle (e.g., areas of precipitation and evaporation), oceanic currents and transport, and river discharge[53]. The MCDC provides SSS retrievals from the 1.4 GHz frequency characteristic of the SMAP MW imager at two resolutions: 40 km and 70 km; values range from 0 to 45 psu. The 70 km SSS product should be used for most scientific purposes as the noise associated with the SSS retrievals is greatly reduced when compared to the 40 km product (Figure 4).

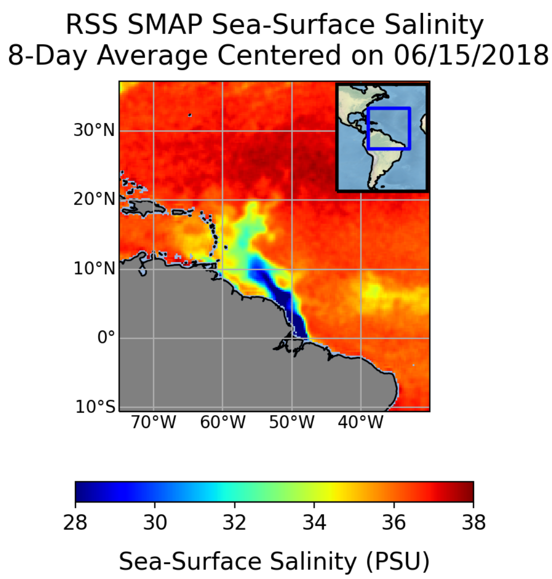

Figure 4 MCDC Sea-Surface Salinity (SSS). SSS from SMAP is averaged over eight days centered on June 15, 2018.

Atmospheric Temperature Profiles over Ocean and Land

Satellite measurements of atmospheric temperature are critical for training and verifying atmosphere-ocean coupled general circulation models (GCMs) to predict future changes to the climate[54]. According to the Intergovernmental Panel on Climate Change (IPCC), under high greenhouse gas emissions scenarios the lower troposphere global average temperatures are predicted to increase by 1.5 °C relative to pre-industrial levels by 2030 to 2052[55]. The MCDC at RSS provides temperature measurements for five layers of the atmosphere over ocean and land: Temperature Lower Troposphere (TLT), Temperature Total Troposphere (TTT), Temperature Middle Troposphere (TMT), Temperature Troposphere Stratosphere (TTS), and Temperature Lower Stratosphere (TLS)[27]. Atmospheric temperatures are calculated from the 50–60 GHz channels of MW sounders; values range from approximately 80 to 310 K depending on the atmospheric layer.

AS-ECV CDRs

RSS has combined select AS-ECV data from multiple MW imagers into a single CDR on a 2.5-degree, global grid for each month from 1987 to present: wind speed, columnar atmospheric water vapor, columnar cloud liquid water, and sea-surface rain rate. During sensor overlap periods, the CDR AS-ECV is determined by averaging the multi-sensor retrievals together into a single gridded map. The CDR additionally includes sea-surface temperature from Reynolds Optimal Interpolation (OI) because the MCDC MW sea-surface temperature record does not extend back to 1987. The CDR was created for trend analysis; for example, Figure 5 shows trend maps of the AS-ECVs from this CDR. A secondary available CDR contains tropospheric and stratospheric temperatures derived from MW sounders, MSU and AMSU, spanning 1979 to present. Figure 6 shows the long-term trends from this CDR: tropospheric temperatures have increased by 0.213 K per decade and stratospheric temperatures have decreased by -0.210 K per decade. The data for the MW imager AS-ECV CDR is located at: https://www.remss.com/climate/Air-Sea-Essential-Climate-Variables/. The data for the MW sounder AS-ECV CDR is located at: https://images.remss.com/msu/msu_time_series.html.

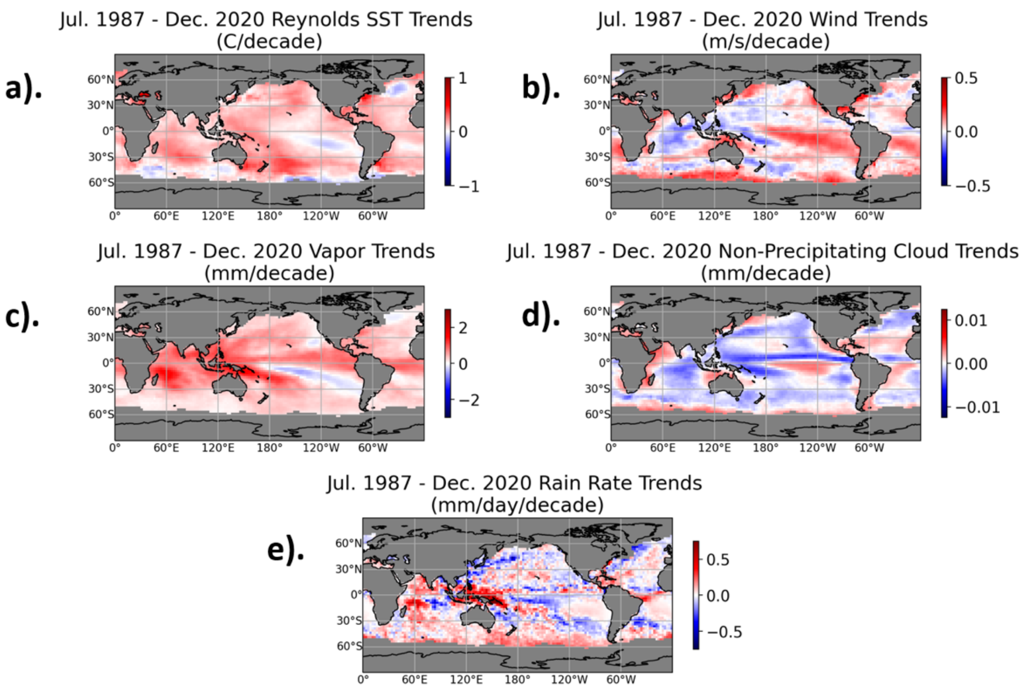

Figure 5 MCDC AS-ECV CDR Trend Maps. Trend maps of monthly MCDC MW imager AS-ECV CDRs for July 1987 to December 2020: sea-surface temperature (SST) (a), wind speed (b), columnar atmospheric water vapor (c), columnar cloud liquid water (d), sea-surface rain rate (e). Monthly values are de-seasonalized to account for monthly variation, i.e., the average monthly value over the entire period for January, February, etc. is subtracted from the observed monthly value before the trend is calculated.

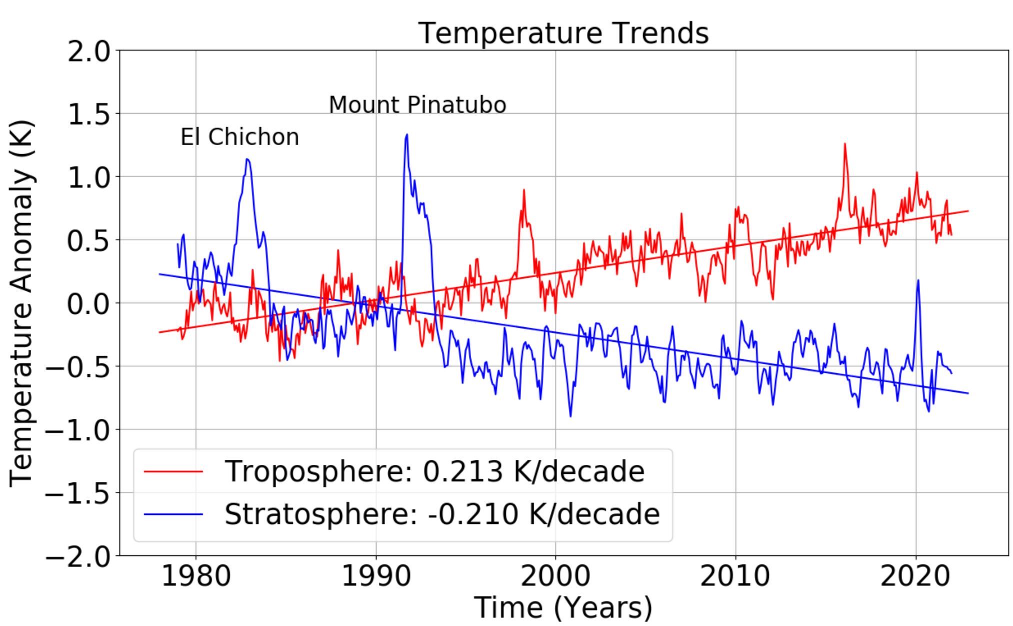

Figure 6 MCDC Temperature CDR Trends. Monthly global average tropospheric (TLT) and stratospheric (TLS) timeseries and trends from January 1979 to January 2022.

Technical Validation

A majority of work completed at RSS revolves around the validation of the MCDC datasets. The following sub-sections provide examples of the technical validation of individual AS-ECV datasets.

Sea-Surface Temperature

The average bias between MCDC MW sub-skin SSTs from TMI and moored buoys is -0.08°C and the standard deviation of the bias is 0.57°C for all collocations from 1998 to 2001[56]. To mitigate the effect of diurnal warming on the bias, SST measurements with corresponding wind speeds less than 6 m/s and between 10 am and 6 pm were excluded from the above statistics. In addition, all retrievals within 25 km of a non-zero rain retrieval were excluded from the bias statistics because undetected rain can cause a warm bias in the MW SSTs. Similar to the TMI validation study, the MCDC MW sub-skin SSTs from AMSR-E (AMSR-2) collocated with moored and drifting buoys, ships, and Coastal-Marine Automated Network in situ SSTs spanning 2002 to 2011 (2012 to 2014) exhibited a bias of -0.05°C (-0.04°C) and standard deviation of 0.48°C (0.55°C)[57,58].

Ocean Wind Speed and Wind Vectors over Ocean and Land

On a global scale, wind speeds between 0–15 m/s from MCDC MW imagers and scatterometers agree with buoy measurements with an error of about 1–1.5 m/s[59,60,61,62]. For higher wind speeds, between 15–25 m/s, accurate in situ measurements from buoys are difficult to obtain because the wind-measuring devices (anemometers) on buoys are impacted by buoy tilting, high sea state, and wave-sheltering[63,64,65]. However, when compared to anemometers mounted high on oil platforms in the North Sea (and therefore not subject to the same ocean effects as buoys) imager and scatterometer wind measurements between 15–25 m/s perform well[66]. Specifically, WindSat exhibited a -0.5 m/s bias and 2.5 m/s standard deviation of the bias at wind speeds of 22 m/s. While the scalar wind speed signal responds with a linear emissivity that does not saturate at extreme winds ~70 m/s[22,67,68], the backscatter signal of wind vector measurements saturates at wind speeds above 35–40 m/s making it difficult to tell the exact wind magnitude[69,70,71]. For MW imagers and scatterometers it is challenging to validate wind speeds above 25–30 m/s because there is a scarcity of data to use as ground truth. That being said, wind information from dropsondes and Stepped-Frequency Microwave Radiometers (SFMRs) on board hurricane-penetrating aircrafts have shown that SMAP can accurately measure wind speeds of up to 70 m/s in tropical cyclones[67,72]. Note that since the TC winds algorithms are trained in TC conditions, they become less accurate in areas where sea-surface temperatures are < 20 °C and wind speed is < 10 m/s. In these conditions, the All-Weather winds product should be used. CCMP should not be used to measure high winds (> 25 m/s) associated with tropical cyclones because the background model winds used in CCMP consistently underestimate winds relative to satellite observations at higher wind speeds, and in some cases tropical cyclones are too spatially-small for the background models to pick up.

Columnar Atmospheric Water Vapor over Ocean

The MCDC water vapor retrievals agree with water vapor measurements from GPS ground stations located on small islands across the globe with mean differences of less than 1 mm between the two[73]. The MCDC water vapor retrievals display a global trend of approximately 1.5% increase per decade[74]. This tracks well with the water vapor increase relative to the increase in global temperature as predicted by the Clausius-Clapeyron equation (~7% increase in water vapor per degree of warming)[75,76,77]. Unfortunately, water vapor is not retrieved in areas of moderate to high rain rate (> 5–10 mm/hr). This can result in a systematic "non-rainy" negative bias in globally-averaged water vapor. Indeed, the MCDC average water vapor retrievals have a small "non-rainy" bias (-0.35–0.15 mm relative to GPS stations)[74]. In the presence of light rain (0–5 mm/hr), RSS is able to retrieve water vapor; however, in this case there is a large positive bias in AMSR-E water vapor measurements (up to 2 mm at rain rates of ≥ 2 mm/hr)[73]. Another issue relates to wind speed: almost every MCDC sensor shows a roughly linear decrease in its water vapor bias relative to GPS stations as wind speed increases[73]. This is potentially due to small errors in the ocean surface model used in the RTM.

Columnar Cloud Liquid Water over Ocean

It is difficult to check the accuracy of MCDC columnar cloud liquid water retrievals against in situ sources because measurements of cloud liquid water over the oceans are sparse and cloud coverage can vary significantly over the large area that the satellite observes. Provided these difficulties, cloud liquid water is validated with probability distribution functions (PDFs) of cloud liquid water for different ranges of sea-surface temperature, wind speed, and atmospheric water vapor. The PDFs have a distinctive shape where the peak of the PDFs is near a cloud liquid water value of 0.025 mm with a half-peak at 0.000 mm. The steeply-sloped left sides correspond to clear-sky conditions when there is little to no cloud liquid water. If the left side half-peak of the stratified PDFs are aligned, it indicates minimal errors in the cloud liquid water measurement, and therefore, minimal contamination or crosstalk from SST, wind speed, or water vapor. Conversely, if the clear-sky portions of the PDFs are not aligned then signals from one of the other geophysical variables in a given scene may be causing an erroneous cloud water signal when there is none. This analysis suggests that the systemic cloud liquid water root-mean-square error is: +/- 0.005 mm[19]. Another source of error could be related to the cloud liquid water vs rain threshold value. In the MCDC algorithm, a cloud is assumed to be raining if the cloud liquid water value is greater than 0.180 mm (i.e., the rain threshold, L_{rain}, is equal to 0.180). It is possible that cloud liquid water may end up being over- (under-) estimated if clouds are precipitating below (above) the threshold of 0.180 mm. However, this threshold was shown to be reasonable[78].

Sea-Surface Rain Rate

The MCDC sea-surface rain rate average bias is 4 mm/yr, or approximately 5×10^{-4} mm/hr, for all measurements of rain rate from TMI compared to the Pacific Marine Environmental Laboratory (PMEL) tropical buoys located between 25°S and 21°N across the years 1997–2011[11]. For the retrieval of rain rate, we use the columnar cloud liquid water as a proxy for rain; for values of cloud liquid water below 0.18 mm, the rain is assumed to be zero[78]. Unaccounted for variations this threshold may produce spurious trends in the rain calculation.

Sea-Surface Salinity

In non-raining scenes and SSTs > 5 °C, the MCDC 70 km SMAP SSS data product has a -0.01 psu bias and a 0.14–0.15 psu standard deviation of the bias when compared to drifting ARGO buoys[1] (a global array of over 3000 floats) and the Hybrid Coordinate Ocean Model (HYCOM)[79,80,81]. In high rain, the ARGO data are not a reliable validation source. This is because the stratification of the upper ocean layer caused by rain results in a sampling mismatch error between the satellite sensor observation, which is within a few centimeters of the surface, and the in-situ observation, which is taken at a depth of 1–5 m[82]. In addition, the MCDC salinity retrievals degrade in cold water, as the 1.4 GHz L-band surface emission loses sensitivity at low SSTs. Other reasons for possible degradation include proximity of the retrieval to land or sea ice and the presence of sun glint or high wind speeds. The effect of the sea ice edge on SSS retrievals has been largely mitigated by a sea ice flag developed by RSS[83].

Atmospheric Temperature Profiles over Ocean and Land

The MCDC TLT dataset shows greater trends in warming (0.21–0.25 K/decade) as compared to radiosonde datasets (0.18–0.20 K/decade)[15]. The University of Alabama-Huntsville (UAH) TLT trends are also smaller than the MCDC TLT trends (0.124 vs 0.174 K/decade for near-global regions and 0.121 vs 0.147 K/decade for tropical regions)[15]. In addition, MCDC TLT is validated with total column water vapor, which is highly correlated with atmospheric temperature over the tropical oceans. In contrast to the radiosonde and UAH TLT biases, the MCDC TLT trend ratio (8%/K) implies slightly less warming than the expected water vapor trend ratio (6.2%/K)[15]. Overall, the MCDC TLT exhibited global errors of ±0.044 K and tropical errors of ±0.034 K in a Monte Carlo analysis that systematically incorporated 400 combinations of errors in TLT[84].

Code Availability

The Radiative Transfer Model code that is used to generate the regressions for the microwave imager retrievals of MCDC AS-ECVs is available upon request from: https://www.remss.com/rtm/. Coefficients for the microwave imager retrieval regressions and scatterometer GMF are available upon request. Weighting functions for the microwave sounder retrievals of atmospheric temperatures are available at: https://data.remss.com/msu/weighting_functions/. In addition, the code for the diurnal warming model used to compute foundation sea-surface temperature is available on the RSS website: https://www.remss.com/research/.

Acknowledgements

Support for the MCDC over the last 40 years has primarily come from NASA's Earth Science Division, from NOAA's Office of Global Programs and National Center for Environment Information Climate Data Record Program, and from the MCDC's Research and Development Program. In addition, we would like to acknowledge the scientists and technical support at Remote Sensing Systems that help create and maintain the datasets presented herein, particularly: Carl Mears, Thomas Meissner, Lucrezia Ricciardulli, Richard Lindsley, Marty Brewer, and Michael Densberger.

[1] The buoy data were collected and made freely available by the International ARGO Program and the national programs that contribute to it; the ARGO Program is part of the Global Ocean Observing System.

Tables

Table 1. Inputs: MW conical scanning imagers used to generate AS-ECV data. SSM/I=Special Sensor Microwave Imager. SSMIS=SSMI Sounder. DMSP=Defense Meteorological Satellite Program. TMI=Tropical Rainfall Measuring Mission (TRMM) Microwave Imager. GMI=Global Precipitation Measurement (GPM) Microwave Imager. AMSR-E & AMSR-2=Advanced Microwave Scanning Radiometers. GCOM-W1=Global Change Observation Mission. SMAP=Soil Moisture Active Passive.

Sensor Name	Satellites	Time Period (years)	Ascending Local Equatorial Time[1]	Frequencies (GHz)	Mean Footprint Resolution (km)[2]	Swath Width (km)
SSM/I[85]	DMSP F08 F10–11 F13–15	1987– Present	06:00 (F08), 17:00–22:00 *Near-Polar Orbit*	19.35 V H 22.24 V 37.00 V H 85.50 V H	56 45 32.5 14	1400
SSMIS[85]	DMSP F16–18	2003– Present	16:30–18:30 *Near-Polar Orbit*	19.35 V H 22.24 V 37.00 V H 91.35 V H	56 45 32.5 14	1700
TMI[86]	TRMM	1997–2015	Variable *Inclined Orbit:* *40°S to 40°N*	10.70 V H 19.35 V 21.30 V H 37.00 V H 85.50 V H	57.5 28 23.5 14 7	758.5
GMI[87]	GPM	2014– Present	Variable *Inclined Orbit:* *60°S to 60°N*	10.65 V H 18.70 V H 23.80 V 36.64 V H 89.00 V H	25.5 14.5 13 12 5.5	930
AMSR-E[88]	Aqua	2002–2011	13:30 *Near-Polar Orbit*	6.925 V H 10.65 V H 18.70 V H 23.80 V H 36.50 V H 89.00 V H	59 40 21.5 25 11 5	1445
AMSR-2[88]	GCOM-W1	2012– Present	13:30 *Near-Polar Orbit*	6.925 V H 7.300 V H 10.65 V H 18.70 V H 23.80 V H 36.50 V H 89.00 V H	48.5 48.5 33 18 15 9.5 4	1450
WindSat[89]	Coriolis	2003–2020	18:10 *Near-Polar Orbit*	6.800 V H 10.70 V H[3] 18.70 V H[3] 23.80 V H 37.00 V H[3]	55 31.5 21.5 25 10.5	950
SMAP[6]	SMAP	2015– Present	18:00 *Near-Polar Orbit*	1.410 V H U	43	1000

[1] Information was obtained from: https://www.remss.com/support/crossing-times/. [2] Information was obtained from: https://www.remss.com/missions/. [3]Fully polarimetric channels.

Table 2. Inputs: MW cross-track scanning sounders used to generate AS-ECV data. MSU=Microwave Sounding Unit. AMSU=Advanced Microwave Sounding Unit. FOV=Sensor Field of View.

Sensor Name	Satellites	Time Period (years)	Ascending Local Equatorial Time[1]	Frequencies (GHz)	Mean Footprint Resolution (km)	Swath Width (km)
MSU[13]	Tiros-N, NOAA-06–12, 14	1978–2005	13:30–20:30 *Near-Polar Orbit*	4 channels: 50.30–57.95 Vx2, Hx2	110	~ 640 (central 5 FOVs)
AMSU-A[13]	NOAA-15, 18–19, MetOp-A, -B, Aqua	1998–Present	13:30–22:00 *Near-Polar Orbit*	11 channels: 52.80–57.29 Vx2, Hx9	48	~ 660 (central 12 FOVs)

[1] Information was obtained from: https://www.remss.com/support/crossing-times/.

Table 3. Inputs: MW scatterometers used to generate AS-ECV data. SeaWinds is a conical scanning "pencil beam" scatterometer, while ASCAT is a cross-track chirping "fan beam" scatterometer. ASCAT=Advanced Scatterometer.

Sensor Name	Satellites	Time Period (years)	Ascending Local Equatorial Time[1]	Frequencies (GHz)	Mean Footprint Resolution (km)	Swath Width (km)
Sea-Winds[90]	Quickbird (*QuikSCAT*) ADEOS-2/ MIDORI-2 (*SeaWinds*)	1999–2009 (*QuikSCAT*) 2002–2003 (*SeaWinds*)	06:00 (*QuikSCAT*) 22:30 (*SeaWinds*) *Near-Polar Orbit*	13.40 V H	44.5 (V) 39 (H)	1800
ASCAT[91]	MetOp -A, -B, -C	2007–Present	21:30 *Near-Polar Orbit*	5.255 V	25 & 50	500 x2

[1] Information was obtained from: https://www.remss.com/support/crossing-times/.

Table 4. Variable definitions for Equations (1) through (17).

Variable Name	Definition
T_B	Top-of-the-atmosphere T_B (K) for a given MW frequency and polarization.
T_A	Top-of-the-ionosphere T_A (K) for a given MW frequency and polarization.
χ	The coefficients of fractional power coming from the orthogonal polarization (cross-polarization coupling).
E_{refl}	Emissivity of the main sensor reflector.
T_{refl}	Temperature (K) of the main sensor reflector.
η	The fraction of received power coming from cold space (spillover).
T_C	Temperature (~2.7 K) of the cosmic microwave background radiation (cold space).
E	Sea-surface emissivity for a given MW frequency and polarization.
T_S	Surface temperature (K).
T_{BU}, T_{BD}	Upwelling and downwelling atmospheric T_B (K).
τ	The total transmissivity through the atmosphere.
$T_{B,scat}$	T_B (K) adjustment that accounts for scattering as opposed to reflections from sea surface.
Ω	Empirical factor term.
h, H	Height (h; km) above Earth' surface and height (H; km) at which the atmospheric absorption is zero.
θ	Angle between the satellite viewing direction and the zenith of the Earth's geoid at boresight (EIA; degrees).
T	Air temperature (K).
α	Atmospheric absorption coefficient for a given MW frequency and polarization.
α_D, α_V, α_L	The three components of atmospheric absorption: dry air, water vapor, liquid cloud water.
ε_L	Dielectric constant of pure (cloud) water which depends on the temperature of the medium.
ρ_V, ρ_L	Water vapor density and cloud liquid water density (kg/m^3).
P	Dry air pressure (kPa).
E_0, ΔE_W, ΔE_φ	Emissivity of the specular ocean surface, isotropic wind-induced emissivity, four Stokes parameters of the wind direction signal.
S	Sea-surface salinity (psu).
W	Wind speed (m/s).
φ	Wind direction relative to azimuthal look (degrees).
m_{1j}, m_{2j}	Measurement of AS-ECV for 1st stage regression and 2nd stage regression.
j, k, l	AS-ECV sea-surface temperature or wind speed index (j), sea-surface temperature 1st stage regression integer value index (k), wind speed 1st stage regression integer value index (l).
a, b, c	Coefficients for AS-ECV non-linear and linear regressions.
w	Linear combination of AS-ECV measurements from 1st stage regression.
z	Zenith optical depth (km).
F	Weighting function for atmospheric layers.
κ	Atmospheric absorption coefficient.
σ_o	The normalized radar cross-section (radar backscatter).
d_0, d_1, d_2	Coefficients of radar backscatter 5th order polynomials.

Table 5. Outputs: Data available at the MCDC. Most products are L(evel) 3 unless specified as L2 or L4. Spatial "Grid" is the spatial sampling in lat/lon degrees. OI=Optimally Interpolated; TC=Tropical Cyclone; CCMP=Cross-Calibrated Multi-Platform.

Variable	Sensors	Spatial		Temporal		Data Format
		Range	Grid	Range	Resolution	
Sea-Surface Temperature	TMI, GMI, AMSR-E, AMSR-2, WindSat	40°S to 40°N (<2002-06-01) Global Ocean (>=2002-06-01)	0.25°	1997–Present	Daily[1], 3-Day, Weekly, Monthly	netCDF4, bytemap
OI Sea-Surface Temperature (MW)	TMI, GMI, AMSR-E, AMSR-2, WindSat	40°S to 40°N (<2002-06-01) Global Ocean (>=2002-06-01)	0.25°	1998–Present	L4 Daily	netCDF4, bytemap
OI Sea-Surface Temperature (MW + IR)	TMI, GMI, AMSR-E, AMSR-2, WindSat, MODIS-Terra, MODIS-Aqua, VIIRS-NPP, VIIRS-N20	Global Ocean	0.09°	2002–Present	L4 Daily	netCDF4, bytemap
Ocean Wind Speed	SSM/I, SSMIS, TMI, GMI, AMSR-E, AMSR-2, SMAP	Global Ocean	0.25°	1987–Present	Daily[1], 3-Day, Weekly, Monthly	netCDF4, bytemap
Ocean Wind Vector[2]	WindSat, QuikScat, Sea-Winds, ASCAT	Global Ocean	0.25°	1999–Present	Daily[1], 3-Day, Weekly, Monthly	bytemap
Ocean TC/ All-Weather Wind Speed	AMSR-E (only TC), AMSR-2, WindSat, SMAP	TC: Tropical Ocean[3] All-Weather: Global Ocean	0.25°	2002–Present	Daily	netCDF4, bytemap
CCMP Ocean Wind Vector[2]	MCDC Wind Vector, Quik-SCAT, ASCAT, Moored Buoys, ERA-Interim	Global Land Global Ocean	0.25°	1988–Present	6-Hourly	netCDF4
Columnar Atmospheric Water Vapor	SSM/I, SSMIS, TMI, GMI, AMSR-E, AMSR-2, WindSat	Global Ocean	0.25°	1987–Present	Daily[1], 3-Day, Weekly, Monthly	netCDF4, bytemap
Columnar Cloud Liquid Water	SSM/I, SSMIS, TMI, GMI, AMSR-E, AMSR-2, WindSat	Global Ocean	0.25°	1987–Present	Daily[1], 3-Day, Weekly, Monthly	netCDF4, bytemap
Sea-Surface Rain Rate	SSM/I, SSMIS, TMI, GMI, AMSR-E, AMSR-2, WindSat	Global Ocean	0.25°	1987–Present	Daily[1], 3-Day, Weekly, Monthly	netCDF4, bytemap
Sea-Surface Salinity	SMAP (40 km & 70 km)	Global Ocean	0.25°	2015–Present	L2 Swath, 8-Day, Monthly	netCDF4
Atmospheric Temperature Profiles	MSU, AMSU	Global Land Global Ocean	2.5°	1978/1987 (TTS)–Present	Monthly	netCDF4, bytemap

[1]Indicates that the daily products include both ascending and descending orbits. [2]Direction+Speed. [3]SST>20°C; Winds>10 m/s.

References

1. Ulaby, F. T. & Long, D. G. *Microwave Radar and Radiometric Remote Sensing* 1st edn (The University of Michigan Press, 2014).
2. Briggs, S. *Status of the Global Observing System for Climate*. GCOS-195 (World Meteorological Organization Geneva, 2015).
3. Martin, S. *An Introduction to Ocean Remote Sensing* 2nd edn (Cambridge University Press, 2014).
4. Wilhet, T. T. & Chang, A. T. C. Retrieval of monthly rainfall indices from microwave radiometric measurements using probability distribution functions. *J. Atm. and Ocean. Tech.* **8,** 118-136 (1990).
5. Wentz, F. J. & Spencer, R. SSM/I rain retrievals within a unified all-weather ocean algorithm. *J. Atmos. Sci.* **55,** 1613-1627 (1998).
6. Entekhabi, D. et al. The Soil Moisture Active Passive (SMAP) mission. *Proc. IEEE* **98,** 704-716 (2010).
7. Robinson, D. et al. *Climate Data Records from Environmental Satellites*. Interim Report. (The National Academy of Sciences, 2004)
8. Wentz, F. J., Ashcroft, P. D. & Gentemann, C. L. Post-launch calibration of the TRMM microwave imager. *IEEE Trans. Geosci. Remote Sens.* **39,** 415-422 (2001).
9. Wentz, F. J. *SSM/I Version-7 Calibration Report*. Report No. 011012 (Remote Sensing Systems, 2013).
10. Wentz, F. J., Gentemann, C. L. & Hilburn, K. A. An analysis of the AMSR-2 brightness temperature calibration. *AGU Fall Meeting Abstracts* (2013).
11. Wentz, F. J. A 17-year climate record of environmental parameters derived from the tropical rainfall measuring mission (TRMM) microwave imager. *J. Clim.* **28,** 6882-6902 (2015).
12. Wentz, F. J. & Draper, D. On-orbit absolute calibration of the global precipitation measurement microwave imager. *J. Atm. and Ocean. Tech.* **33,** 1393-1412 (2016).
13. Mears, C. M. & Wentz, F. J. Construction of the Remote Sensing Systems V3.2 atmospheric temperature records from the MSU and AMSU microwave sounders. *J. Atm. and Ocean. Tech.* **26,** 1040-1056 (2009).
14. Mears, C. M. & Wentz, F. J. Construction of the RSS V3.2 Lower-Tropospheric Temperature Dataset from the MSU and AMSU Microwave Sounders. *J. Atm. and Ocean. Tech.* **26,** 1493-1509 (2009).
15. Mears, C. A. & Wentz, F. J. A satellite-derived lower tropospheric atmospheric temperature dataset using an optimized adjustment for diurnal effects. *J. Clim.* **30,** 7695-7718 (2017).
16. Ricciardulli, L. & Manaster, A. Intercalibration of ASCAT scatterometer winds from Metop-A, -B, and -C for a stable climate data record. *Rem. Sens.* **13,** 3678 (2021).
17. Meissner, T., Wentz, F. J. & Le Vine, D. M. The salinity retrieval algorithms for the NASA Aquarius version 5 and SMAP version 3 releases. *Rem. Sens.* **10,** 1121 (2018).
18. Wentz, F. J. & Meissner, T. *Algorithm Theoretical Basis Document (ATBD), Version 2, AMSR Ocean Algorithm*. Report No. 121599A-1 (Remote Sensing Systems, 2000).
19. Wentz, F. J. A well-calibrated ocean algorithm for special sensor microwave imager. *J. Geophys. Res.* **102,** 8703-8718 (1997).
20. Meissner, T. & Wentz, F. J. An updated analysis of the ocean surface wind direction signal in passive microwave brightness temperatures. *IEEE Trans. Geosci. Remote Sens.* **40,** 1230-1240 (2002).
21. Meissner, T. & Wentz, F. J. The complex dielectric constant of pure and sea water from microwave satellite observations. *IEEE Trans. Geosci. Remote Sens.* **42,** 1836-1849 (2004).
22. Meissner, T. & Wentz, F. J. The emissivity of the ocean surface between 6 and 90 GHz over a large range of wind speeds and Earth incidence angles. *IEEE Trans. Geosci. Remote Sens.* **50,** 3004-3026 (2012).
23. Meissner, T., Wentz, F. J. & Ricciardulli, L. The emission and scattering of L-band microwave radiation from rough ocean surfaces and wind speed measurements from the Aquarius sensor. *J. Geophys. Res. Oceans* **119,** 6499-6522 (2014).
24. Wentz, F. J. & Meissner T. Atmospheric absorption model for dry air and water vapor at microwave frequencies below 100 GHz derived from spaceborne radiometer observations. *Radio Sci.* **51,** 381-391 (2016).
25. Wentz, F. J. & Meissner, T. *Algorithm Theoretical Basis Document (ATBD), Supplement 1, AMSR Ocean Algorithm*. Report No. 1051707 (Remote Sensing Systems, 2007).
26. Meissner, T. & Wentz, F. J. Ocean retrievals for WindSat: Radiative transfer model, algorithm, validation. *Proceedings of OCEANS 2005 MTS/IEEE*. IEEE 130-133 (2005).
27. Mears, C. A. *Climate Algorithm Theoretical Basis Document (C-ATBD), RSS Version 3.3 MSU/AMSU-A Mean Layer Atmospheric Temperature*. Report No. CDRP-ATBD-0201 (NOAA Climate Data Record (CDR) Program, 2013).
28. Fu, Q., Johanson, C. M., Warren, S. G. & Seidel, D. J. Contribution of stratospheric cooling to satellite-inferred tropospheric temperature trends. *Nature* **429,** 55-58 (2004).
29. Wentz, F. J. & Smith, D. K. A model function for the ocean-normalized radar cross section at 14 GHz derived from NSCAT observations. *J. Geophys. Res. Oceans* **104,** 11499-11514 (1999).
30. Ricciardulli, L. & Wentz, F. J. A scatterometer geophysical model function for climate-quality winds: QuikSCAT Ku-2011. *J. Atm. and Ocean. Tech*. **32,** 1829-1846 (2015).
31. Kosaka, Y. & Xie, S. P. Recent global-warming hiatus tied to equatorial Pacific surface cooling. *Nature* **501,** 403-407 (2013).
32. Lorenc, A. C. A global three-dimensional multivariate statistical interpolation scheme. *Mon. Wea. Rev.* **109,** 701-721 (1981).
33. Reynolds, R. W. & Smith, T. M. Improved global sea surface temperature analyses using optimum interpolation. *J. Clim.* **7,** 929-948 (1994).

34. Kawai, Y. et al. Satellite-based high-resolution global optimum interpolation sea surface temperature data. *J. Geophys. Res.* **111,** 17 (2006).
35. Fairall, C. W. et al. Cool-skin and warm-layer effects on sea surface temperature. *J. Geophys. Res. Oceans* **101,** 1295-1308 (1996).
36. Wentz, F. J., Wentz, K. & Lindsley, R. *A Diurnal Warming Model for the Sub-Skin Temperature of the Ocean*. Report No. 04262021 (Remote Sensing Systems, 2021).
37. Capotondi, A. & Ricciardulli, L. The influence of pacific winds on ENSO diversity. *Scientific Reports* **11,** 1-11 (2021).
38. Zhisheng, A. et al. Global monsoon dynamics and climate change. *Ann. Rev. Earth Plan. Sci.* **43,** 29-77 (2015).
39. Meissner, T. & Wentz, F. J. Wind vector retrievals under rain with passive satellite microwave radiometers. *IEEE Trans. Geosci. Remote Sens.* **47,** 3065-3083 (2009).
40. Meissner, T., Ricciardulli, L. & Manaster A. Tropical cyclone wind speeds from AMSR and WindSat: Algorithm development and testing. *Remote Sens.* **13,** 1641 (2021).
41. Manaster, A., Ricciardulli, L. & Meissner, T. Tropical cyclone winds from WindSat, AMSR2, and SMAP: Comparison with the HWRF model. *Remote Sens.* **13,** 2347 (2021).
42. Atlas, R. et al. A cross-calibrated, multiplatform ocean surface wind velocity product for meteorological and oceanographic applications. *Bull. Amer. Meteor. Soc.* **92,** 157-174 (2011).
43. Mears, C. A. et al. A near real time version of the Cross Calibrated Multiplatform (CCMP) ocean surface wind velocity data set. *J. Geophys. Res. Oceans* **124,** 6997-7010 (2019).
44. Espinoza, V., Waliser, D. E., Guan, B., Lavers, D. A. & Ralph, F. M. Global analysis of climate change projection effects on atmospheric rivers. *Geophys. Res. Let.* **45,** 4299-4308 (2018).
45. Payne, A. E. et al. Responses and impacts of atmospheric rivers to climate change. *Nat. Rev. Earth Env.* **1,** 143-157 (2020).
46. Held, I. M. & Soden, B. J. Water vapor feedback and global warming. *Ann. Rev. Ener. and Env.* **25,** 441-475 (2000).
47. Forster, P. et al. in *Climate Change 2021: The Physical Science Basis. Contribution of Working Group I to the Sixth Assessment Report of the Intergovernmental Panel on Climate Change.* Ch. 7 (Cambridge University Press, 2021).
48. Lee, W. H., Iacobellis, S. F. & Somerville, R. C. J. Cloud radiation forcings and feedbacks: General circulation model tests and observational validation. *J. Clim.* **10,** 2479-2496 (1997).
49. Guan, B., Molotch, N. P., Waliser, D. E., Fetzer, E. J. & Neiman, P. J. Extreme snowfall events linked to atmospheric rivers and surface air temperature via satellite measurements. *Geophys. Res. Lett.* **37,** 6 (2010).
50. Dettinger, M. D., Ralph, F. M., Das, T., Neiman, P. J. & Cayan, D. R. Atmospheric rivers, floods and the water resources of California. *Water* **3,** 445-478 (2011).
51. Zhiseng A. et al. Global monsoon dynamics and climate change. *Ann. Rev. Earth Plan. Sci.* **43,** 29-77 (2014).
52. Byrne, M. P., Pendergrass, A. G., Rapp, A. D. & Wodzicki, K. R. Response of the intertropical convergence zone to climate change: location, width, and strength. *Curr. Clim. Chg. Rep*. **4,** 355-370 (2018).
53. Gierach, M. M., Vazquez-Cuervo J., Lee T. & Tsontos, V. M. Aquarius and SMOS detect effects of an extreme Mississippi River flooding event in the Gulf of Mexico. *Geophys. Res. Lett.* **40,** 1-6 (2013).
54. Santer, B. D. et al. Tropospheric warming over the past two decades. *Scientific Reports* **7,** 1-6 (2017).
55. Allen M. R. et al. in: *Special Report: Global Warming of 1.5°C*. Summary for Policymakers (World Meteorological Organization, Geneva, Switzerland, 2018).
56. Gentemann, C. L., Wentz, F. J., Mears, C. A. & Smith, D. K. In situ validation of Tropical Rainfall Measuring Mission microwave sea surface temperatures. *J. Geophys. Res.* **109,** 9 (2004).
57. Gentemann, C. L. Three way validation of MODIS and AMSR-E sea surface temperatures. *J. Geophys. Res. Oceans* **119,** 2583-2598 (2014).
58. Gentemann, C. L. & Hilburn, K. A. In situ validation of sea surface temperatures from the GCOM-W1 AMSR2 RSS calibrated brightness temperatures. *J. Geophys. Res. Oceans* **120,** 3567-3585 (2015).
59. Mears, C. A., Smith, D. K. & Wentz, F. J. Comparison of special sensor microwave imager and buoy-measured wind speeds from 1987 to 1997. *J. Geophys. Res. Oceans* **106,** 11719-11729 (2001).
60. Ebuchi, N., Graber, H. C. & Caruso, M. J. Evaluation of wind vectors observed by QuikSCAT/SeaWinds using ocean buoy data. *J. Atm. and Ocean. Tech.* **19,** 2049-2062 (2002).
61. Verspeek, J. et al. Validation and calibration of ASCAT using CMOD5.n. *IEEE Trans. Geosci. Remote Sens*. **48,** 386-395 (2010).
62. Wentz F. J. et al. Evaluating and extending the ocean wind climate data record. *IEEE J. Sel. Top. Appl. Earth Obs. and Remote Sens*. **10,** 2165-2185 (2017).
63. Large, W. G., Morzel, J. & Crawford, G. B. Accounting for surface wave distortion of the marine wind profile in low-level ocean storms wind measurements. *J. Phys. Oceanogr*. **25,** 2959-2971 (1995).
64. Skey, S. G. P. & Miles, M. D. Advances in buoy technology for wind/wave data collection and analysis. *IEEE OCEANS'99* (1999).
65. Howden, S. et al. Hurricane Katrina winds measured by a buoy-mounted sonic anemometer. *J. Atm. and Ocean. Tech*. **25,** 607-616 (2008).
66. Manaster, A., Ricciardulli, L. & Meissner, T. Validation of high ocean surface winds from satellites using oil platform anemometers. *J. Atm. and Ocean. Tech.* **36,** 803-818 (2019).

67. Meissner, T., Ricciardulli, L. & Wentz, F. J. Capability of the SMAP mission to measure ocean surface winds in storms. *Bull. Amer. Meteor. Soc.* **98,** 1660-1677 (2017).
68. Jones, W. L., Black, P. G., Delnore, V. E. & Swift, C. T. Airborne microwave remote-sensing measurements of Hurricane Allen. *Science* **214,** 274-280 (1981).
69. Jones, W. L. et al. Evaluation of the Seasat wind scatterometer. *Nature* **294,** 704-707 (1981).
70. Fernandez, D., Chang, P., Carswell, J., Contreras, R. & Chu, T. Spectral behavior of the ocean surface backscatter and the atmospheric boundary layer at C- and Ku-band under high wind and rain conditions. *IEEE International Geoscience and Remote Sensing Symposium (IGARSS)* (2006).
71. Sapp, J. W. et al. Airborne co-polarization and cross-polarization observations of the ocean-surface NRCS at C-band. *IEEE Trans. Geosci. Remote Sens.* **54,** 5975-5992 (2016).
72. Yueh, S. et al. Applications of SMAP data to retrieval of ocean surface wind and salinity. *Remote Sensing of the Oceans, Sea Ice, Coastal Waters, and Large Water Regions, International Society for Optics and Photonics* **9999,** 117-124 (2016). SPIE.
73. Mears, C. A., Wang, J., Smith, D. & Wentz, F. J. Intercomparison of total precipitable water measurements made by satellite-borne microwave radiometers and ground-based GPS instruments. *J. Geophys. Res.: Atms.* **120,** 2492-2504 (2015).
74. Mears, C. A. et al. Construction and uncertainty estimation of a satellite-derived total precipitable water data record over the world's oceans. *Earth and Space Sci.* **5,** 197-210 (2018).
75. Trenberth, K. E., Fasullo, J. & Smith, L. Trends and variability in column-integrated atmospheric water vapor. *Clim. Dyna.* **24,** 741-758 (2005).
76. Wang, J., Dai, A. & Mears, C. A. Global water vapor trend from 1988 to 2011 and its diurnal asymmetry based on GPS, radiosonde, and microwave satellite measurements. *J. Clim.* **29,** 5205-5222 (2016).
77. Mears, C. A., Santer, B. D., Wentz, F. J., Taylor, K. E & Wehner, M. F. Relationship between temperature and precipitable water changes over tropical oceans. *Geophys. Res. Lett.* **34,** 5 (2007).
78. Hilburn, K. & Wentz, F. J. Intercalibrated passive microwave rain products from the Unified Microwave Ocean Retrieval Algorithm (UMORA). *J. Appl. Meteor. Climatol.* **47,** 778-794 (2008).
79. Meissner, T., Wentz, F. J., Manaster, A. & Lindsley, R. *NASA/RSS SMAP Salinity: Version 4.0 Validated Release*. Report No. 082219 (Remote Sensing Systems, 2019).
80. Chassignet, E. P. et al. US GODAE: Global Ocean Prediction with the HYbrid Coordinate Ocean Model (HYCOM). *Oceanography* **22,** 64-75 (2009).
81. Argo. Argo float data and metadata from Global Data Assembly Centre (Argo GDAC). *SEANOE* https://www.seanoe.org/data/00311/42182/ (2000).
82. Boutin, J. et al. Satellite and in situ salinity: Understanding near-surface stratification and subfootprint variability. *Bull. Amer. Meteor. Soc.* **97,** 1391-1407 (2016).
83. Meissner, T. & Manaster, A. SMAP salinity retrievals near the sea-ice edge using multi-channel AMSR2 brightness temperatures. *Remote Sensing*. **13,** 5120 (2021).
84. Mears, C. A., Wentz, F. J., Thorne, P. & Bernie, D. Assessing uncertainty in estimates of atmospheric temperature changes from MSU and AMSU using a Monte-Carlo estimation technique. *J. Geophys. Res.* **116,** 16 (2011)**.**
85. Fennig, K., Schroder, M., Andersson, A. & Hollmann, R. A fundamental climate data record of SMMR, SSM/I, and SSMIS brightness temperatures. *Earth Syst. Sci. Data* **12,** 647-681 (2020).
86. Kummerow, C., Barnes, W., Kozu, T., Shiue, J. & Simpson J. The Tropical Rainfall Measuring Mission (TRMM) sensor package. *J. Atm. and Ocean. Tech.* **15,** 809-817 (1998).
87. Draper, D. W., Newell, D. A., Wentz, F. J., Krimchansky, S. & Skofronick-Jackson, G.M. The Global Precipitation Measurement (GPM) Microwave Imager (GMI): Instrument overview and early on-orbit performance. *IEEE J. Selec. Topics App. Earth Obs. Rem. Sens.* **8,** 3452-3462 (2015).
88. Du, J. et al. Inter-calibration of satellite passive microwave land observations from AMSR-E and AMSR2 using overlapping FY3B-MWRI sensor measurements. *Remote Sens.* **6,** 8594-8616 (2014).
89. Gaiser, P. W. et al. The WindSat spaceborne polarimetric microwave radiometer: Sensor description and early orbit performance. *IEEE Trans. Geo. Rem. Sens.* **42,** 2347-2361 (2004).
90. Long, D. G. & Draper, D. Evaluating the effect of rain on SeaWinds scatterometer measurements. *J. Geophys. Res.* **109,** (2004).
91. Figa-Saldaña, J. et al. The advanced scatterometer (ASCAT) on the meteorological operational (MetOp) platform: A follow on for European wind scatterometers. *Can J. Remote Sensing* **28,** 404-412 (2002).